Deep Resources Engineering 1 (2024) 100001

Contents lists available at ScienceDirect

Deep Resources Engineering

journal homepage: www.keaipublishing.com/en/journals/deepre/

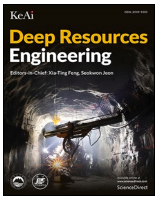

Full Length Article

Numerical analysis of thermo-hydromechanical process related to deep geological radioactive repository

Jian-Fu Shao [a,b,*], Zhan Yu [a,c], Zaobao Liu [c], Minh-Ngoc Vu [d], Gilles Armand [d]

[a] *University of Lille, CNRS, EC Lille, LaMcube, UMR9013, 59000 Lille, France*
[b] *Institut Universitaire de France (IUF), France*
[c] *Key Laboratory of Ministry of Education on Safe Mining of Deep Metal Mines, College of Resources and Civil Engineering, Northeastern University, Shenyang 110819, China*
[d] *Andra, Chatenay Malabry, France*

ARTICLE INFO

Keywords:
Radioactive waste
Geological disposal
Thermo-hydromechanical coupling
Callovo-oxfordian claystone
Damage and cracking
Phase-field method

ABSTRACT

This paper addresses numerical analysis of thermo-hydromechanical processes in the context of deep geological disposal of radioactive waste. The emphasis is put on modeling of damaged zones induced by excavation, pore pressure and temperature changes. The theoretical background of thermo-poroelasticity for saturated porous media is first recalled. The framework for modeling initiation and evolution of induced cracks is then presented by using a variational approach of phase-field method. A specific model with two crack phase fields and considering thermo-hydromechanical interaction is proposed. A particular attention is paid on the description of shear cracks. The proposed model is implemented in the standard finite element method. An example of application is finally presented on the analysis of thermo-hydromechanical responses and cracked zones evolution around a typical disposal repository in the context of French concept for high level waste disposal.

1. Introduction

Deep geological disposal is considered as a possible solution of radioactive waste management in many countries. In this context, it is crucial to investigate thermo-hydromechanical responses of all involved components and their interfaces during construction, operation period and after closure. The host rock plays an essential role to insure long-term safety of disposal. In France, the Callovo-Oxfordian claystone (COx) has been selected as geological barrier for both intermediate-level long-lived waste (IL-LLW) and high-level waste (HLW) [1]. A high number of experimental studies at sample scale have been performed to investigate the main properties of the COx claystone, including basic deformation and failure behavior [2–4], time-dependent deformation [5–7], water saturation effect [8], thermal effect [9,10], influence of mineral composition [11], thermal cracking in saturated condition [6,12–15], and other aspects.

On the other hand, a series of in situ experiments have been and are being performed in the Meuse/Haute-Marne Underground Research Laboratory (URL) [1,15–17]. The goals of those experiments are the characterization of thermo-hydromechanical responses of the host rock during the different phases of geological disposal, and to demonstrate the feasibility of constructing and operating a disposal site in the COx claystone formation. For example, several heating experiments from small-scale to full-scale have been conducted in the URL to study the THM responses of the COx claystone in quasi real conditions, and to assess different aspects related to the conception and design optimization of disposal facilities [1,15–18]. Indeed, pore water pressure in surrounding saturated claystone increases due to temperature rise caused by heat emission of HLW packages. This is a consequence of the thermal expansion coefficient difference between pore water ($2.3 \times 10^{-4}\ K^{-1}$ at 20˚C and $7.2 \times 10^{-4}\ K^{-1}$ at 90˚C) and solid skeleton ($1.5 \times 10^{-5}\ K^{-1}$ for the COx claystone) [6,12,13]. Owing to the low permeability of the host rock ($1.0 \times 10^{-21}\ m^2$ to $2.0 \times 10^{-20}\ m^2$) [19,20], the induced pressure built-up is followed by a slow water flow phase. It is then important to verify possible cracking process in the host rock due to the pore pressure rise.

In this study, the emphasis is put on the analysis of cracking processes in the near field of the repository under coupled thermo-hydromechanical conditions. During the last decades, various numerical methods have been developed for modeling crack initiation and

---

Peer review under responsibility of Editorial Board of Deep Resources Engineering.

* Corresponding author at: University of Lille, CNRS, EC Lille, LaMcube, UMR9013, 59000 Lille, France.
E-mail address: jian-fu.shao@polytech-lille.fr (J.-F. Shao).

https://doi.org/10.1016/j.deepre.2024.100001
Received 14 September 2023; Received in revised form 18 January 2024; Accepted 22 January 2024

propagation. For instance, we can mention Extended finite element method (XFEM), based on global enrichment technique to represent discontinuity caused by cracks (fractures) [21,22], Enriched finite element method (EFEM) using a local enrichment solution of elementary sharp functions [23–26]. In these methods, the transition from diffuse deformation to localized cracking remains an open issue. Moreover, it is also a hard task to perform three-dimensional thermo-hydromechanical calculations with the presence of multiple cracks. More recently, based on the variational principle of fracture mechanics [27], a new numerical solution, called phase-field method, has been developed [28,29]. With the approximation of sharp fractures by a regularized smear crack density field, this method is able to easily deal with the nucleation and propagation of cracks. In this framework, various specific models have been developed for addressing cracking in plastic materials [30–32], under dynamic loading etc. The phase-field method has also been applied to cracking modeling with thermo-hydromechanical coupling [33–35].

In this paper, we shall present a short summary of numerical modeling framework of thermo-hydromechanical responses and induced cracking processes in the context of deep geological disposal of radioactive waste. The basic relations of thermo-poroelasticity are first recalled. The key issues of the phase-field method are then presented. We propose further a specific phase-field model for saturated rocks by considering both tensile and shear cracks. Influences of pore fluid pressure and thermal stress are taken into account. An example of application is finally presented about the thermo-hydromechanical modeling of a HLW disposal unit.

2. Fundamental relations of thermo-poro-elasticity

In this section, the fundamental relations are presented for the analysis of thermo-poro-elastic coupling. For the sake of clarity, only saturated cases are considered. These relations can be easily extended to elastic-plastic materials after introducing specific models for modeling plastic deformation.

We consider here the elastic behavior of porous medium saturated by a single fluid phase, water in the present case. The constitutive relations of thermo-poro-elastic theory [36,37] can be expressed as:

$$\begin{cases} \boldsymbol{\sigma} - \boldsymbol{\sigma}^0 = \mathbb{C}_b : \boldsymbol{\varepsilon}^e - \boldsymbol{B}(p - p^0) - \boldsymbol{A}_b\theta \\ p - p_0 = M(-\boldsymbol{B} : \boldsymbol{\varepsilon}^e + \dfrac{m}{\rho_f^0}) + 3\alpha_m M\theta \\ s - s_0 = s_m^0 m + \boldsymbol{\alpha}_b : (\boldsymbol{\sigma} - \boldsymbol{\sigma}^0) - (3\alpha_m - \boldsymbol{B} : \boldsymbol{\alpha}_b)(p - p_0) + \dfrac{C_\sigma^b}{T_0}\theta \end{cases} \tag{1}$$

$\boldsymbol{\sigma}^0$, p_0, s_0, T_0 and ρ_f^0 denote the values of stress, fluid pressure, entropy, temperature and volumetric density of fluid at the initial reference configuration. The variation of temperature is defined as $\theta = T - T_0$. $\mathbb{C}_b$ is the forth order elastic stiffness tensor in drained condition. The scalar coefficient M is the Biot modulus and $\boldsymbol{B}$ is the second order tensor of Biot coefficients. $\boldsymbol{\alpha}_b$ and $\boldsymbol{A}_b$ are two second order tensors respectively for thermal dilatation and thermo-elastic coupling coefficients in drained condition. C_σ^b is the volumetric specific heat for constant stress under drained condition. The coefficient α_m denotes the differential thermal dilation of saturated porous medium. In the case of isotropic materials, one has $\mathbb{C}_b^0 = 3K_b\mathbb{J} + 3\mu_b\mathbb{K}$, with K_b^0 and μ_b^0 being the drained bulk and shear modulus respectively. The other coefficients are also simplified as follows: $\boldsymbol{B} = b\boldsymbol{\delta}$, $\boldsymbol{\alpha_b} = \alpha_b\boldsymbol{\delta}$ and $\boldsymbol{A}_b = 3K_b\alpha_b\boldsymbol{\delta}$. The Biot modulus is given by $1/M = (b - \phi)/K_m + \phi/K_f$, with K_m being the bulk modulus of solid matrix, K_f that of fluid and ϕ porosity. The differential thermal dilation coefficient is expressed $\alpha_m = (b - \phi)\alpha_b + \phi\alpha_f$ with the thermal dilation coefficient of the fluid α_f.

By applying the momentum balance equation, Darcy's fluid conduction law, fluid mass conservation, Fourier heat conduction law and energy balance relation, one gets the following governing equations for boundary values problems:

$$\begin{cases} div\boldsymbol{\sigma} + \mathbf{f}_b = 0 \\ \operatorname{div}\left(\dfrac{\boldsymbol{\kappa}}{\mu_f} : \nabla p\right) = \dfrac{1}{M}\dfrac{\partial p}{\partial t} + \dfrac{\partial(\boldsymbol{B} : \boldsymbol{\epsilon})}{\partial t} - 3\alpha_m\dfrac{\partial\theta}{\partial t} \\ \operatorname{div}(\boldsymbol{\lambda} : \nabla\theta) = \dfrac{1}{C_\epsilon^b}\dfrac{\partial\theta}{\partial t} - 3\alpha_m T_0\dfrac{\partial p}{\partial t} + T_0\dfrac{\partial(\boldsymbol{A}_b : \boldsymbol{\epsilon})}{\partial t} \end{cases} \tag{2}$$

In these relations, $\boldsymbol{\kappa}$ and $\boldsymbol{\lambda}$ are respectively the permeability and heat conductivity tensors. μ_f denotes the dynamic viscosity of fluid while C_ϵ^b is the specific heat of porous medium with constant volume and drained condition. It is noticed that the heat convection term of the fluid flow is neglected in the third relation. After knowing specific boundary and initial conditions, these governing equations can be solved for given boundary values problems.

3. Description of damage and cracking

In the context of geological disposal of radioactive waste, damaged and cracked zones can be induced by excavation, changes of temperature and increase of water and gas pressure. It is therefore crucial to describe the nucleation and evolution of such zones in short and long terms. As mentioned above, among various numerical methods developed for modeling cracking processes, the phase-field method provides an efficient tool for the description of transition from diffuse damage and localized cracks. In this section, the formulation of a specific phase-field model for rock materials considering thermo-hydromechanical coupling is presented.

We consider a saturated porous medium that occupies the volume Ω with its external boundary surface $\partial\Omega$. It is subjected to the body force $\mathbf{f}_b$ in Ω, the surface force $\mathbf{t}_N$ on the part of external boundary $\partial\Omega_f$ and the prescribed displacement $\overline{\mathbf{u}}$ on the complementary part of external boundary $\partial\Omega_u$. The porous medium is also subjected to the fluid flux $\overline{\boldsymbol{\omega}}$ on the external boundary $\partial\Omega_\omega$ and to the prescribed fluid pressure $\overline{p}$ on $\partial\Omega_p$. Moreover, a heat flux $\overline{\mathbf{q}}$ is applied onto the external boundary $\partial\Omega_q$ and a temperature change $\overline{\theta}$ is prescribed on $\partial\Omega_\theta$. The problem to be solved is to determine the displacement (strain and stress), pore fluid pressure and temperature fields, as well as the process of initiation and propagation of cracks within Ω during the entire loading history.

3.1. Regularized description of crack evolution

The phase-field method is developed from the variational principle of fracture mechanics proposed in [27]. Its numerical implementation is completed by introducing approximation of sharp crack topology by regularized smeared crack distribution [28,29]. For this purpose, the crack state is represented by a scalar-valued auxiliary variable $d(\mathbf{x})$, taking the unit value on crack surface and vanishes at intact state. The total area of sharp cracks surfaces in Ω is accordingly approximated by the volume integration of a crack surface density function:

$$A_\Gamma = \int_{\Gamma^k} \mathrm{d}A \Rightarrow A_{\Gamma_l}(d) = \int_\Omega \gamma(d, \nabla d)\mathrm{d}\Omega \tag{3}$$

The function $\gamma(d, \nabla d)$ represents the crack surface area per unit volume (m^2/m^3). It is assumed that $\gamma(d, \nabla d)$ at each material point not only depends on d but also on its gradient ∇d. Such a non-local formulation allows a regularized description of localization of damage into narrow zones (smeared cracks). Among different possible choices [38], the following one is widely used and adopted here [29].

$$\gamma(d, \nabla d) = \frac{d^2}{2l_d} + \frac{l_d}{2}|\nabla d|^2 \tag{4}$$

l_d is a length scale parameter controlling the width of smeared cracks.

The crack phase-field $d(\mathbf{x}, \mathbf{t})$ is solution of the following boundary value problem:

$$\begin{cases} d - l_d^2 \operatorname{div}(\nabla d) = 0 \text{ in } \Omega \\ d(\mathbf{x}, t) = 1 \text{ on } \Gamma \\ \nabla d(\mathbf{x}, t) \cdot \mathbf{n} = 0 \text{ on } \partial\Omega \end{cases} \tag{5}$$

On the other hand, the above boundary value problem can be seen as equivalent to the following variational formulation:

$$d(\boldsymbol{x}, t) = \operatorname{Arg}\left\{ \inf_{d \in W_{\Gamma_l(t)}} A_{\Gamma_l}(d) \right\}, \quad W_{\Gamma_l(t)} = \{ d | d(\boldsymbol{x}, t) = 1, \boldsymbol{x} \in \Gamma(t) \} \tag{6}$$

According to the variational principle [27], the evolution of d is governed by the minimization of a total energy functional. This one is generally composed of two terms, respectively representing the stored (or available) energy and the needed energy for the nucleation and propagation of cracks in Ω:

$$E(\boldsymbol{u}, d) = \int_\Omega w_s(\boldsymbol{u}, d) \mathrm{d}V + \mathscr{D}_c \tag{7}$$

The stored energy w_s is generally composed of elastic strain energy w_e and that due to plastic deformation. Its particular expression is related to specific constitutive models adopted. As an example, for materials described by an elastic-plastic model with hardening, one can writes [33,39,40]:

$$E(\boldsymbol{\varepsilon}(\boldsymbol{u}), \boldsymbol{\varepsilon}^p, \boldsymbol{V}^p, d) = \int_\Omega w_e(\boldsymbol{\varepsilon}, \boldsymbol{\varepsilon}^p, \boldsymbol{V}^p, d) \mathrm{d}V + \int_\Omega \beta(d) \int_0^t \varphi_p(\dot{\boldsymbol{\varepsilon}}^p, \dot{\boldsymbol{V}}^p) \mathrm{d}\tau \mathrm{d}V + \mathscr{D}_c \tag{8}$$

$\boldsymbol{\varepsilon}^p$ denotes plastic strain tensor, φ_p plastic dissipation potential, and $\boldsymbol{V}^p$ set of plastic hardening variables. The function $\beta(d)$ defines the coupling between crack evolution and plastic deformation. The dissipated energy for crack propagation $\mathscr{D}_c$ can be written in the following general form:

$$\mathscr{D}_c = \int_\Omega g_c \gamma(d, \nabla d) \mathrm{d}V \tag{9}$$

g_c is called the critical toughness and represents the energy used for the creation of unit area of crack surface (J/m^2). By minimization of the total energy functional, one gets the governing equations of phase-field evolution:

$$\begin{cases} -\dfrac{\partial w_e}{\partial d} + \beta'(d) w_p^0 - g_c \delta_d \gamma = 0, & \dot{d} > 0, \text{ in } \Omega \\ -\dfrac{\partial w_e}{\partial d} + \beta'(d) w_p^0 - g_c^\alpha \delta_d \gamma \le 0, & \dot{d} = 0, \text{ in } \Omega \\ \dfrac{\partial \gamma}{\partial \nabla d} . \mathbf{n} = 0, & \text{on } \delta\Omega \end{cases} \tag{10}$$

$\delta_d \gamma$ denotes the variational derivative. w_p^0 represents the energy related to plastic strain per unit volume.

3.2. A specific phase-field model for saturated rocks

Most rocks are subjected to compression-dominating stresses and exhibits complex cracking modes. Tensile, shear and mixed cracks are widely observed [41,42]. In order to conveniently deal with such mixed-mode cracks, in this specific model, two phase fields are introduced to represent two basic families of cracks, i.e. tensile and shear cracks respectively represented by the phase-field d^t and d^s. Thus, the total crack surface area $\Gamma_{l_d}(d)$ is defined by:

$$\Gamma_{l_d} = \Gamma_{l_d}^t(d^t) + \Gamma_{l_d}^s(d^s) = \int_\Omega \{ \gamma^t(d^t, \nabla d^t) + \gamma^s(d^s, \nabla d^s) \} dV \tag{11}$$

The same density function as that given in (4) is used for both families of cracks:

$$\gamma^\alpha(d^\alpha, \nabla d^\alpha) = \frac{1}{2} \left\{ \frac{1}{l_d} (d^\alpha)^2 + l_d \nabla d^\alpha . \nabla d^\alpha \right\}; \quad \alpha = t, s \tag{12}$$

Accordingly, the energy density requested to the propagation of cracks becomes:

$$\mathscr{D}_c(d^t, d^s, \nabla d^t, \nabla d^s) = \int_\Omega g_c^t \gamma^t(d^t, \nabla d^t) + g_c^s \gamma^s(d^s, \nabla d^s) \mathrm{d}V \tag{13}$$

g_c^t and g_c^s are respectively the critical toughness for tensile and shear cracks.

3.2.1. Elastic stored energy

In order to take into account the effects of pore fluid pressure and temperature change on crack evolution, by using the constitutive relations in (1), the elastic free energy of an intact porous medium can be conveniently expressed in the following form:

$$w_e^0(\boldsymbol{\varepsilon}^e, p, \theta) = \frac{1}{2} \boldsymbol{\sigma}_b : \boldsymbol{\varepsilon}^e + \frac{1}{2} \frac{(p - p_0)^2}{M} - \frac{1}{2} \frac{C_\sigma^b}{T_0} \theta^2 \tag{14}$$

$\boldsymbol{\sigma}^b$ is the Biot (elastic) effective stress tensor given by:

$$\boldsymbol{\sigma}^b = (\boldsymbol{\sigma} - \boldsymbol{\sigma}^0) + \boldsymbol{B}(p - p_0) \tag{15}$$

In most rocks, the evolution of tensile cracks is generally induced by tensile effective stress. For this reason, the Biot effective stress tensor is decomposed into a positive (tensile) part and a negative (compression) part such as: $\boldsymbol{\sigma}^b = \boldsymbol{\sigma}^{b+} + \boldsymbol{\sigma}^{b-}$. The decomposition is completed by using the spectral operators $\mathbb{P}_\sigma^\pm$ [43]:

$$\begin{cases} \boldsymbol{\sigma}^{b+} = \mathbb{P}_\sigma^+ : \boldsymbol{\sigma}^b \\ \boldsymbol{\sigma}^{b-} = \mathbb{P}_\sigma^- : \boldsymbol{\sigma}^b \end{cases} \tag{16}$$

Accordingly, the elastic strain energy is rewritten as follows:

$$w_e^0(\boldsymbol{\varepsilon}^e, p, \theta) = w_e^{0+}(\boldsymbol{\varepsilon}^e) + w_e^{0-}(\boldsymbol{\varepsilon}^e) + \frac{1}{2} \frac{(p - p^0)^2}{M} - \frac{1}{2} \frac{C_\sigma^b}{T_0} \theta^2 \tag{17}$$

with

$$\begin{cases} w_e^{0+} = \dfrac{1}{2} \boldsymbol{\sigma}^{b+} : \boldsymbol{\varepsilon}^e \\ w_e^{0-} = \dfrac{1}{2} \boldsymbol{\sigma}^{b-} : \boldsymbol{\varepsilon}^e \end{cases} \tag{18}$$

It is further assumed that the tensile crack affects the positive stresses-related part of the elastic strain energy while the shear crack influences the negative stresses-related part. For the sake of simplicity, the effects of induced cracks on Biot modulus M and specific heat C_σ^b are here neglected. Therefore, the elastic strain energy for cracked materials is expressed as:

$$w_e(\boldsymbol{\varepsilon}^e, p, \theta, d^t, d^s) = h_t(d^t) w_e^{0+} + h_s(d^s) w_e^{0-} + \frac{1}{2} \frac{(p - p_0)^2}{M} - \frac{1}{2} \frac{C_\sigma^b}{T_0} \theta^2 \tag{19}$$

h_t and h_s are two degradation functions of elastic energy due to crack evolution. The following widely used form is here adopted:

$$h_\alpha(d^\alpha) = (1 - k)(1 - d^\alpha)^2 + k; \quad \alpha = t, s \tag{20}$$

The small positive constant k is introduced to avoid numerical fluctuation when the material is fully broken ($d^\alpha = 1$).

3.2.2. Evolution laws

Putting the emphasis to thermo-poroelastic coupling, plastic deformation is not considered in this study. Thus, according to (10), the evolution of two crack fields are described by the following equations:

$$\begin{cases} -h'_t(d^t)w^0_{e+} - g^t_c\left\{\dfrac{1}{l_d}d^t - l_d div(\nabla d^t)\right\} = 0, \quad \dot{d}^t > 0 \\ -h'(d^s)w^0_{e-} - g^s_c\left\{\dfrac{1}{l_d}d^s - l_d div(\nabla d^s)\right\} = 0, \quad \dot{d}^s > 0 \end{cases} \tag{21}$$

Accordingly, the tensile crack evolution is driven by the elastic strain energy w^0_{e+} which is a function of tensile (positive) Biot effective stresses $\boldsymbol{\sigma}^{b+}$. At the same time, the evolution of shear crack should be controlled by the elastic strain energy w^0_{e-} attributed to compressive (negative) Biot effective stresses $\boldsymbol{\sigma}^{b-}$. However, this result issued from the variational approach cannot correctly reflect the shear cracking mechanism in rocks. Indeed, it is known that the shear cracking is generally controlled by both the maximum shear stress and compressive mean stress. The classical Mohr-Coulomb criterion is widely used in rock mechanics to represent such physical mechanism. In the context of shear crack evolution, a hybrid model is here proposed. The MC criterion is reformulated in an energy form [43], and an alternative driving force w^s_- is defined as follows:

$$w^s_- = \frac{1}{2G}\langle\frac{\langle\sigma^t_1\rangle_- - \langle\sigma^t_3\rangle_-}{2cos\varphi} + \frac{\langle\sigma^t_1\rangle_- + \langle\sigma^t_3\rangle_-}{2}tan\varphi - c\,\rangle^2_+ \tag{22}$$

with the bracket $\langle . \rangle_\pm$ such as:

$$\begin{cases} \langle a\rangle_+ = a, \quad \langle a\rangle_- = 0, \quad a \geq 0 \\ \langle a\rangle_+ = 0, \quad \langle a\rangle_- = a, \quad a < 0 \end{cases} \tag{23}$$

σ^t_1 and σ^t_3 are the major and minor Terzaghi effective principal stress [44,45]. c and φ denote the local cohesion and friction angle of closed cracks. By substituting w^s_- for Equations (21), the evolution criteria for two crack phase fields are now expressed as:

$$\begin{cases} -h'_t(d^t)w^0_{e+} - g^t_c\left\{\dfrac{1}{l_d}d^t - l_d div(\nabla d^t)\right\} = 0, \quad \dot{d}^t > 0 \\ -h'(d^s)w^s_- - g^s_c\left\{\dfrac{1}{l_d}d^s - l_d div(\nabla d^s)\right\} = 0, \quad \dot{d}^s > 0 \end{cases} \tag{24}$$

Considering crack evolution as an irreversible process and inspired by previous studies [46], the following energy history functionals are introduced:

$$\begin{cases} \mathscr{H}^t(t) = max[w^0_{e+}(\tau)]_{\tau\in[0,t]} \\ \mathscr{H}^s_-(t) = max[w^s_-(\tau)]_{\tau\in[0,t]} \end{cases} \tag{25}$$

Consequently, the evolution equations for two crack fields become:

$$\begin{cases} -h'_t(d^t)\mathscr{H}^t - g^t_c\left\{\dfrac{1}{l_d}d^t - l_d div(\nabla d^t)\right\} = 0 \\ -h'_s(d^s)\mathscr{H}^s_- - g^s_c\left\{\dfrac{1}{l_d}d^s - l_d div(\nabla d^s)\right\} = 0 \end{cases} \tag{26}$$

4. Numerical implementation in finite element method

In the context of tensile and shear cracks in thermo-hydromechanical problems, five coupled physical fields should be determined. By using the framework of finite element method, the weak forms of static equilibrium, hydraulic and heat diffusion are expressed as:

$$\int_\Omega \delta\boldsymbol{\varepsilon} : \mathbb{C}^b(d^t, d^s) : \boldsymbol{\varepsilon} dV - \int_\Omega \delta\boldsymbol{\varepsilon} : (\delta p)\boldsymbol{I}\, dV - \int_\Omega \delta\boldsymbol{\varepsilon} : (3\alpha_b K_b(d^t, d^s)T)\boldsymbol{I}\, dV = \int_{\Omega_f} \boldsymbol{t}.\delta\boldsymbol{u} dS \tag{27}$$

$$\begin{aligned} \int_\Omega \frac{\boldsymbol{k}(d^t)}{\mu}\nabla p.\nabla(\delta p)dV \quad = \quad & \int_{\Omega_\omega} \frac{\boldsymbol{k}(d^t)}{\mu}\delta p.\nabla p\bar{n}dS - \int_\Omega \frac{1}{M}\frac{\partial p}{\partial t}\delta p dV \\ & - \int_\Omega b\frac{\partial\varepsilon_{kk}}{\partial t}\delta p dV + \int_\Omega 3\alpha_m\frac{\partial\theta}{\partial t}\delta p dV \end{aligned} \tag{28}$$

$$\begin{aligned} \int_\Omega \lambda\nabla T.\nabla(\delta\theta)dV \quad = \quad & \int_{\Omega_q} \lambda\delta T\nabla T.\bar{n}dS - \int_\Omega C^b_\varepsilon\frac{\partial\theta}{\partial t}\delta\theta dV - \int_\Omega (3\alpha_b K_b(d^t, d^s)T_0)\frac{\partial\varepsilon_{kk}}{\partial t}\delta\theta dV \\ & + \int_\Omega (3\alpha_m T_0)\frac{\partial p}{\partial t}\delta\theta dV + \int_\Omega \frac{\boldsymbol{k}(d^t)}{\mu}\nabla p.(C_p\nabla\theta)\delta\theta dV \end{aligned} \tag{29}$$

$\mathbb{C}^b(\boldsymbol{d}^t, \boldsymbol{d}^s)$ is the drained elastic stiffness tensor of cracked material. This one is affected by the evolution of cracks. Based on the degradation function adopted in (20), one gets:

$$\mathbb{C}_b(d^t, d^s) = \left\{h_t(d^t)\mathbb{P}^+_\sigma + h_s(d^s)\mathbb{P}^-_\sigma\right\} : \mathbb{C}^0_b \tag{30}$$

with $\mathbb{C}^0_b$ being the drained elastic stiffness tensor of undamaged material. The permeability tensor of cracked porous media K_b is also affected by crack growth. For the sake of simplicity but without loosing generality, it is assumed that permeability is mainly affected by open tensile crack. The following simple relation is here used:

$$\boldsymbol{k}(d^t) = \boldsymbol{k}_0\exp(\beta_k d^t) \tag{31}$$

$\boldsymbol{k}_0$ is the initial permeability tensor of intact porous medium and the parameter β_k controlling its evolution. For the sake of simplicity, the dynamic viscosity μ and thermal conductivity tensor λ are assumed not to be affected.

On the other hand, based on the governing equations (26), the weak forms for the evolution of tensile and shear crack fields can be written as:

$$\int_\Omega \{\left(g^t_c/l_d + 2\mathscr{H}_t\right)d^t\delta d^t + g^t_c\nabla d^t\cdot\nabla(\partial d^t)\,\}dV = \int_\Omega 2\mathscr{H}_t\partial d^t dV \tag{32}$$

$$\int_\Omega \{\left(g^s_c/l_d + 2\mathscr{H}^s_-\right)d^s\delta d^s + g^s_c\nabla d^s\cdot\nabla(\partial d^s)\,\}dV = \int_\Omega 2\mathscr{H}^s_-\partial d^s dV \tag{33}$$

Based on elementary approximation with suitable shape functions for each field, together with an implicit time discretization scheme, the following discrete systems of equations for coupled thermo-hydromechanical (THM) problems are obtained:

$$\begin{cases} \mathbf{R}_{uu}\Delta\mathbf{U} + \mathbf{C}_{up}\Delta\mathbf{P} + \mathbf{C}_{uT}\Delta\mathbf{T} = \Delta\mathbf{F}_e \\ C_{pu}\Delta\mathbf{U} + (\Delta\mathbf{t}\mathbf{R}_{pp} + \mathbf{M}_{pp})\Delta\mathbf{P} + \mathbf{C}_{pT}\Delta\mathbf{T} = \Delta\mathbf{t}(-\mathbf{R}_{pp}\mathbf{P} + \Delta\mathbf{F}_\omega) \\ C_{Tu}\Delta\mathbf{U} + \mathbf{C}_{Tp}\Delta\mathbf{P} + (\Delta\mathbf{t}\mathbf{R}_{TT} + \mathbf{M}_{TT})\Delta\mathbf{T} = \Delta\mathbf{t}(-\mathbf{R}_{TT}\mathbf{T} + \Delta\mathbf{F}_q) \end{cases} \tag{34}$$

The solution at each time step leads to the increment nodal values of displacement $\triangle\mathbf{U}$, pore pressure $\triangle P$ and temperature $\triangle T$. The detailed expression of all matrices can be found Appendix A.

In a similar way, the discrete system of equations for the tensile and shear crack fields can be written as:

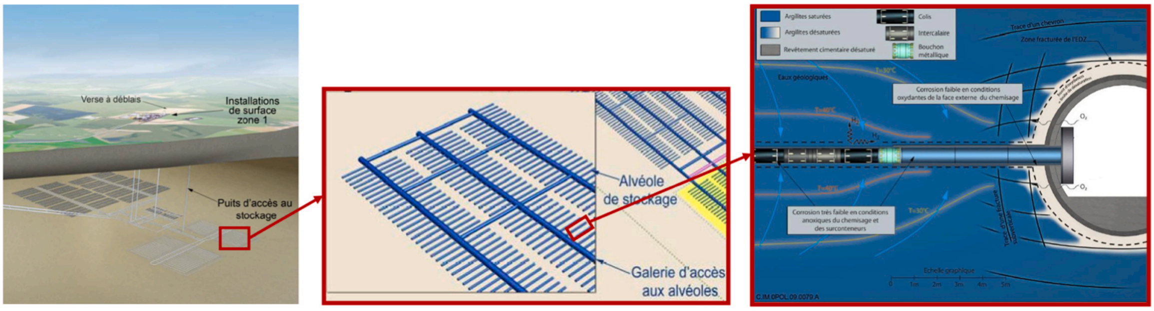

Fig. 1. French concept of a HLW disposal cell.

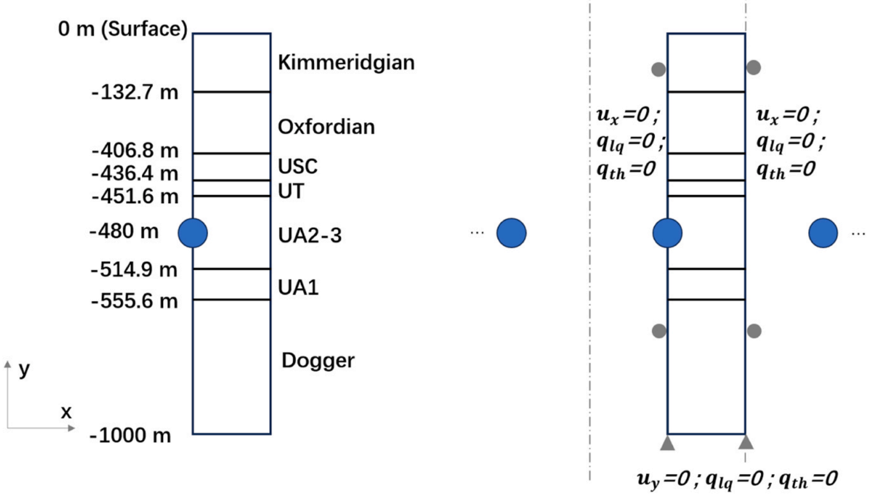

Fig. 2. Geometry and boundary conditions of HLW disposal test [48].

$$\begin{cases} \mathbf{K}_{d^t}\mathbf{d}^t = \mathbf{F}_{d^t} \\ K_{d^t} = \int_\Omega \left\{ \left(g_c^t/l_d + 2\mathscr{H}_t \right) \mathbf{N}_p^T \mathbf{N}_p + g_c^t l_d \mathbf{B}_p^T \mathbf{B}_p \right\} dV \\ F_{d^t} = \int_\Omega 2\mathscr{H}_t \mathbf{N}_p^T dV \end{cases} \tag{35}$$

$$\begin{cases} \mathbf{K}_{d^s}\mathbf{d}^s = \mathbf{F}_{d^s} \\ K_{d^s} = \int_\Omega \left\{ \left(g_c^s/l_d + 2\mathscr{H}_-^s \right) \mathbf{N}_p^T \mathbf{N}_p + g_c^s l_d \mathbf{B}_p^T \mathbf{B}_p \right\} dV \\ F_{d^s} = \int_\Omega 2\mathscr{H}_-^s \mathbf{N}_p^T dV \end{cases} \tag{36}$$

It is obvious that the thermo-hydromechanical solutions are influenced by the evolution of crack fields. Inversely, the propagation of cracks is controlled by the variations of stress, pore pressure and temperature. It is needed to set up an efficient numerical algorithm to solve such strongly coupled and non-linear systems. Inspired by previous studies [28,47], an Alternate Minimization (AM) strategy is used here. Namely, the THM solutions are first determined based on the crack fields obtained at the previous time step. They are then used for the determination of crack fields. All the solutions are updated through an iterative loop until the suitable convergence criteria are reached.

5. Application to HLW disposal analysis [48]

In this section, an example of application is presented on numerical analysis of thermo-hydromechanical responses and induced crack evolution in the context of French concept of High-Level Waste (HLW) disposal [48–50].

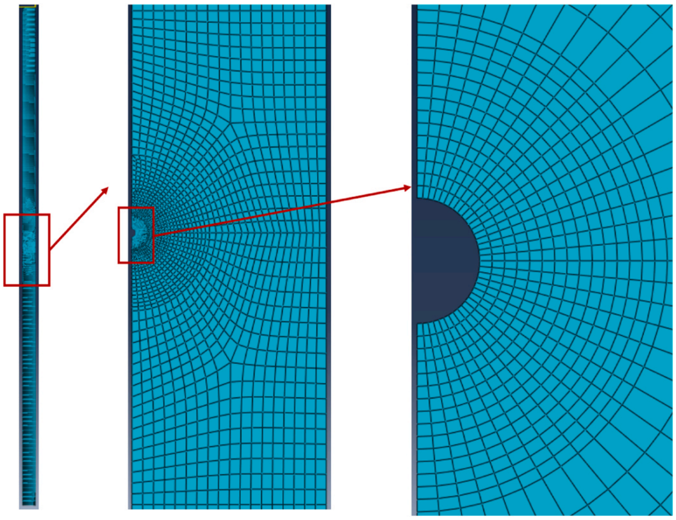

Fig. 3. Mesh strategy of HLW disposal test.

5.1. Input data of HLW disposal concept

The French concept for the HLW disposal area involves the construction of parallel, sub-horizontal micro-tunnels, known as HLW disposal cells, as shown in Fig. 1. These cells are drilled from access drifts located in the COx formation. The design of the french HLW disposal has been performed by 3D simulation. However, as the cell length is much higher than its diameter, 2D plane strain is enough to reproduce all main

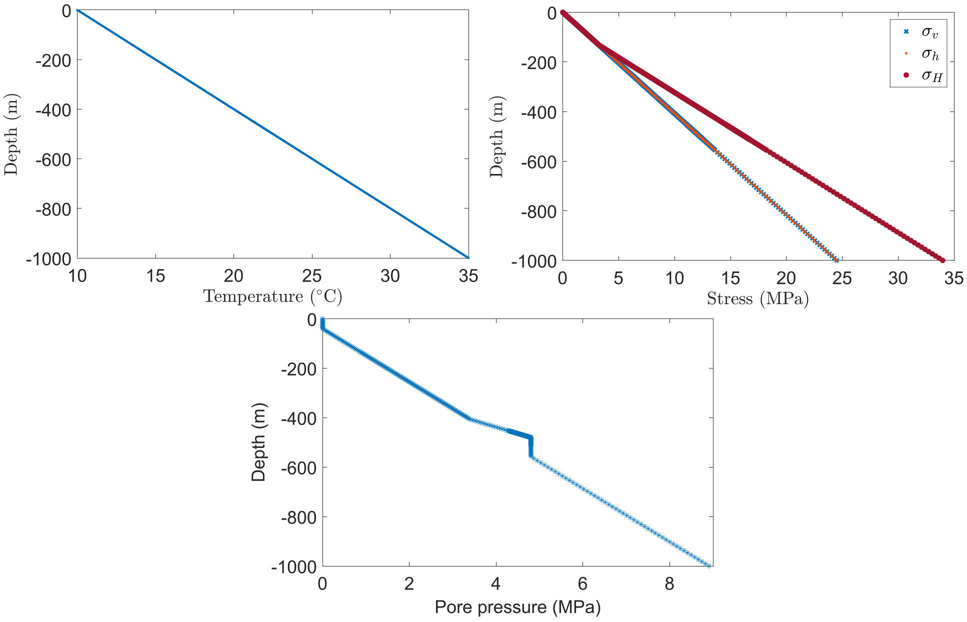

Fig. 4. Initial conditions for temperature, stress and pore pressure according to depth.

Table 1
Boundary conditions at the borehole wall.

Process (period)	Thermal conditions	Hydraulic conditions	Mechanical conditions
Excavation (t = 0 → 24 h)	No flow	$p_0 \rightarrow 0.1$ MPa	$\sigma_0 \rightarrow 0$ MPa
Holding (t = 24 h → 2 years)	No flow	No flow	Free
Heating (t = 2 years → 1000 years)	Applied power of HLW	No flow	Free

phenomenological THM reponses of the repository [50]. For two-dimensional simulations, the geometry domain involves a single disposal cell to leverage symmetry, considering the architecture of the HLW repository comprising multiple parallel cells.

As depicted in Fig. 2, the domain represents a vertical cross-section of the repository at the mid-plane of the HLW disposal cells, and it is approximated as a plane strain problem. Since the half cell-to-cell distance (lateral extent) is set equal to 25 m, the left and right edges of the domain are treated as symmetry boundaries. The micro-tunnel is equipped with steel casing and filling material, which are simplified as boundary conditions, and detailed explanations of these conditions will be provided later.

The domain spans from the surface of the earth (depth of 0) to a depth of 1000 m, with the HLW repository situated within the COx formation at a depth of 480 m. The diameter of HLW cell is 1 m. The dimensions of the various geological layers are taken into consideration and are illustrated in Fig. 2. To mesh the studied domain, 5876 quadrilateral elements with 6196 nodes are utilized, as illustrated in Fig. 3. The area surrounding the HLW cell is subjected to refinement, with 36 elements specifically defined around the demi-cell.

The vertical profiles of the initial conditions are presented in Fig. 4. The overburden exhibits a natural geothermal gradient of 0.025°C/m, and the surface temperature is 10°C. This results in a temperature of 22°C at a depth of 480 m.

At a given depth, the vertical stress is calculated as the weight of the overburden using the approximation: Vertical stress σ_v (MPa) from density profile is given by $\sigma_v = 0.0245 \times$ depth (unit of depth is meter). The minimum horizontal stress σ_h is equal to σ_v. And the maximum horizontal stress σ_H (MPa) is equal to the vertical stress in the Kimmeridgian and $1.3 \times \sigma_h$ from top COx.

Similarly, the initial pore pressure p_0 (in MPa) exhibits a gradient with respect to the depth:

$$p_0 = -0.0093(\text{depth}) - 0.3748 \tag{37}$$

except for the geological layer of COx claystone (depth $\in [-406.8, -555.6]$), where an overpressure is observed in the in-situ measurement. To account for this overpressure, additional line segments are used to describe the variation. Consequently, an initial pore pressure of 4.8 MPa is recorded at a depth of 480 m.

The far-field boundary conditions of the HLW cell are defined as shown in Fig. 2 (right). Specifically: .

- The upper edge has free displacement, with a fixed temperature of 10°C, and a fixed pore pressure of 0.1 MPa.
- The bottom edge has fixed displacement in the y direction, and there is no flow for the thermal and hydraulic fields.
- The lateral edges have fixed displacement in the x direction, and there is no flow for the thermal and hydraulic fields.

The near-field boundary conditions of the HLW cell vary according to

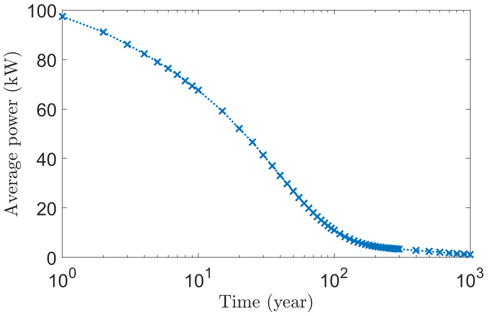

Fig. 5. Evolution of applied thermal load according to the time.

Table 2
Material parameters of the geological layers.

Notation	Unit	KIM	OXF	USC	UT	UA23	UA1	DOG
$E_\perp$	GPa	3.6	30	12.8	8.5	7	10	30
$\mu_{\perp\parallel}$	–	0.3	0.3	0.3	0.3	0.3	0.3	0.3
b	–	0.6	0.75	0.8	0.8	0.8	0.8	0.6
ϕ	%	13	13	15	18	18	18	10
$k_\perp^0$	$10^{-20}\ m^2$	10	10^4	1.3	1.3	1.3	1.3	10^2
ρ_s	kg/m^3	2450	2470	2480	2386	2386	2386	2470
$\lambda_\perp$	W/m/K	1.1	2.3	1.8	1.4	1.25	1.6	2.3
α_s	10^{-5} 1/K	2.2	0.45	1.28	1.28	1.28	1.28	0.45
C_s^p	J/kg/K	1024	925	790	790	790	790	925

Table 3
Anisotropy ratio of the geological layers.

Notation	KIM	OXF	USC	UT	UA23	UA1	DOG
$E_\parallel/E_\perp$	1	1	1	1.5	1.5	1.5	1
$\mu_{\perp\parallel}/\mu_{\parallel\parallel}$	1	1	1	1.5	1.5	1.5	1
$k_\parallel^0/k_\perp^0$	1	1	3	3	3	3	1
$\lambda_\parallel/\lambda_\perp$	1	1	1	1.5	1.5	1.5	1

Table 4
Parameter of phase field model.

Parameters	Value
Material toughness	$g_c^t = 2000$ N/m; $g_c^s = 2000$ N/m
Friction angle	$\varphi = 15^\circ$
Cohesion	$c = 0.1$ MPa
Scale length	$l_d = 0.15$ m
Permeability variation	$\eta_k = 20$

different process phases, namely excavation, holding, and heating phases, as shown in Table 1. During the excavation phase, the initial stress reduces to 0 MPa, and the initial pore pressure reduces to atmospheric pressure at the borehole wall. Subsequently, there is a 2-year holding phase after the excavation, during which the hydraulic condition becomes impermeable due to the installation of steel casing. The heating phase commences in the 2nd year after excavation. During this phase, heating power is generated from the HLW repository stored in the borehole.

The thermal history is based on a HLW (so-called COG-800) package. According to the ANDRA concept, 42 of these packages will be stored in the 100 m long cell. After being installed in the cell, the thermal load will gradually decrease over time, as demonstrated in Fig. 5 (See detail of the average power data in Appendix B)). Two cases are considered to investigate in this work: 1) The packages are installed after allowing them to cool down for 85 years; 2) The packages are installed after waiting only 55 years.

The material parameters for the various geological layers are provided in Table 2. Among them, COx claystone consists of USC, UT, and UA. UT and UA are considered a transversely isotropic material, whereas the USC and other layers are considered isotropic materials. The corresponding anisotropy ratios for the transversely isotropic COx claystone materials are provided in Table 3. Therefor, the shear modulus $G_{\perp\parallel}$ (GPa) of transversely isotropic material can be approximated by Saint-Venant's formula:

$$\frac{1}{G_{\perp\parallel}} = \frac{1}{E_\perp} + \frac{1}{E_\parallel} + 2\frac{\mu_{\perp\parallel}}{E_\perp} \tag{38}$$

According to previous studies [29,51,52], the scale length l_d is typically chosen to be 1 to 3 times the size of the element expected to be damaged. In this work, we adopt l_d to be thrice the size of the studied element, $l_d = 0.15$ m. Toughness parameters, friction angle, cohesion, and permeability variation parameters are defined based on previous numerical studies conducted on COx claystone [43,53]Table 4.

In this work, the standard parameters of water are employed. For simplicity, the following parameters are treated as constants: the bulk modulus of water, $K_f = 2.2$ GPa; the density of water, $\rho_f = 1000$ kg/m^3; and the heat capacity of water, $C_p^f = 4180$ J/kg/K. The water's dynamic viscosity, μ_f (Pa · s), varies with temperature (°C) and is given by:

$$\mu_f(T) = 4.2844 \times 10^{-5} + \left(0.157(T + 64.993)^2 - 91.296\right)^{-1} \tag{39}$$

And the volumetric thermal expansion of water (1/°C) is also dependent on temperature (°C):

$$\alpha_f(T) = -6T^4 + 1660T^3 - 197796T^2 + 16862446T - 64319951 \tag{40}$$

Therefore, for the equivalent parameter of the porous medium, we make the assumption that the heat capacity can be calculated as follows:

$$(\rho C_p)_{eq} = (1-\phi)\left(\rho_s C_p^s\right) + \phi\left(\rho_f C_p^f\right) \tag{41}$$

5.2. Simulation results

The simulation focuses on the long-term evolution of temperature and pore pressure during the heating phase. Specifically, the study aims

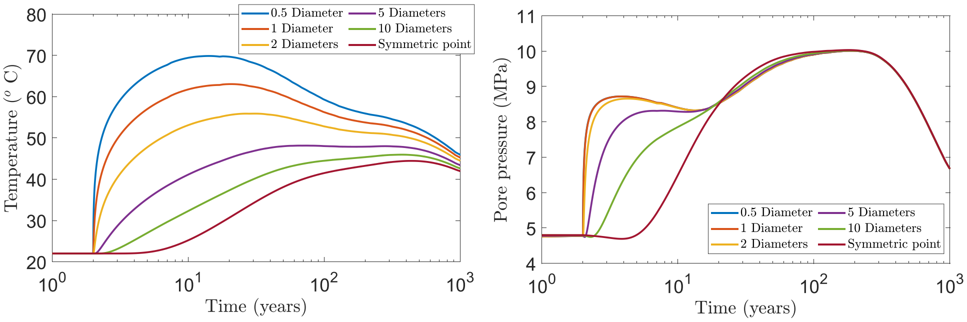

Fig. 6. Evolution of temperature (left) and pore pressure (right) at the different study points: 0.5 diameter, 1 diameter, 2 diameters, 5 diameters, 10 diameters and symmetric point (Case of 85-year cooling down).

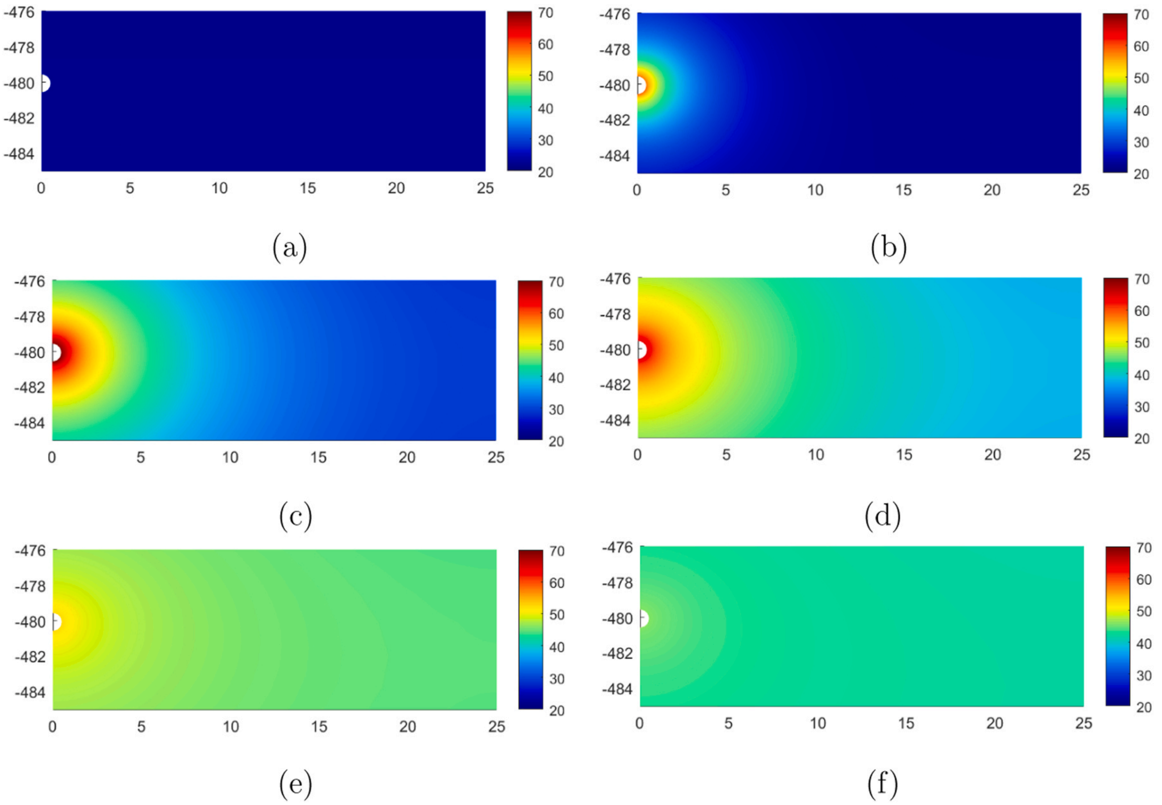

Fig. 7. Distributions of temperature at different time of the heating phase: a) t = 0 year of heating; b) t = 1 year of heating; c) t = 13 years of heating; d) t = 48 years of heating; e) t = 500 years of heating; f) t = 1000 years of heating (Case of 85-year cooling down).

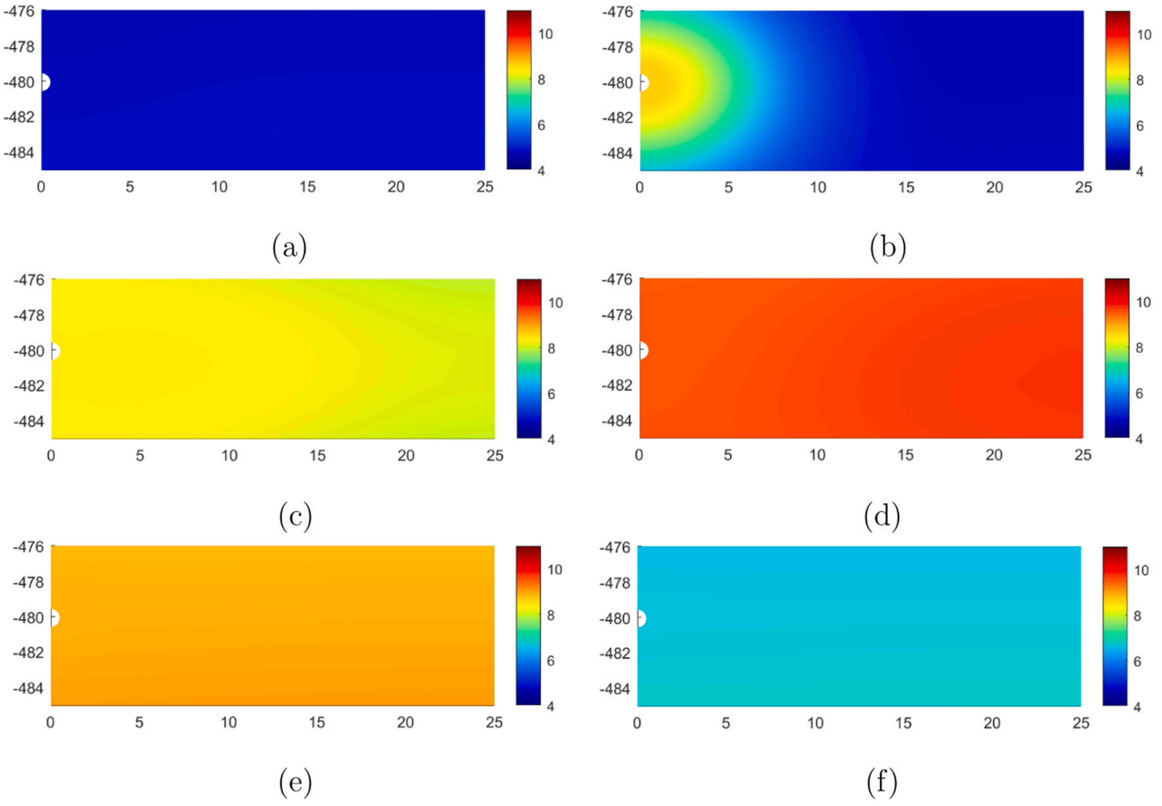

Fig. 8. Distributions of pore pressure at different time of the heating phase: a) t = 0 year of heating; b) t = 1 year of heating; c) t = 13 years of heating; d) t = 48 years of heating; e) t = 500 years of heating; f) t = 1000 years of heating (Case of 85-year cooling down).

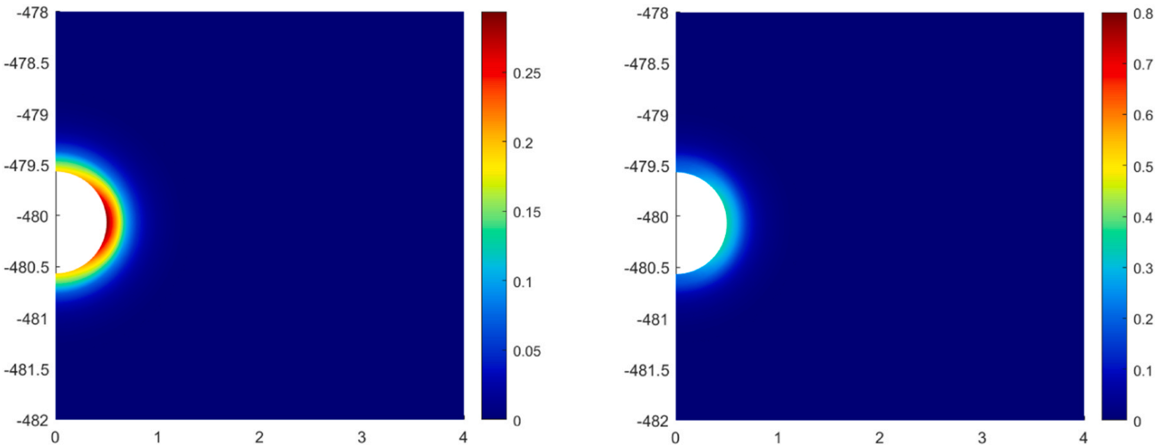

Fig. 9. Distribution of shear damage (left) and tensile damage (right) after the excavation.

to understand the THM behavior of COx claystone induced by the heating of the HLW repository. This investigation pays particular attention to the coupling processes between cells over an extended heating period.

For this purpose, various points with different horizontal distances are selected for analysis. In Fig. 6, the simulation results for the case of an 85-year cooling period of the HLW package are presented. The left side of Fig. 6 illustrates the temperature variations over a span of 1000 years at six different points: 0.5 diameter away from the center point of the cell, 1 diameter away, 2 diameters away, 5 diameters away, 10 diameters away, and the symmetric point situated at the right edge of the study domain. Notably, the temperature reaches its peak at the 13th year of heating, with the maximum value of approximately 70˚C observed at the point located 0.5 diameter away from the center. Subsequently, the temperature begins to decline after the 13th year due to a sharp reduction in heating power.

Fig. 7 depicts the temperature distributions at several significant moments of time. Starting from the initial state, shown in Fig. 7(a), a temperature gradient around the borehole wall becomes apparent during the initial 45 years of heating, as illustrated in Fig. 7(b-d). In particularly, Fig. 7(c) captures the moment when the temperature reaches its peak value in proximity to the borehole.

As time progresses, the temperature gradually diminishes after the 13th year due to the reduction in heating power. Consequently, the temperature gradient diminishes, evident at the 500-year mark of heating, as depicted in Fig. 7(e). By the end of the simulation (after 1000 years of heating), this temperature gradient has nearly disappeared, as shown in Fig. 7(f). Nevertheless, the temperature does not return to its initial value over 1000 years; instead, an average temperature of approximately 45˚C is distributed within the study area between the two heating cells.

Similarly, the right side of Fig. 6 illustrates the pore pressure variations over a 1000-year span at the same six study points. Unlike the temperature evolution, the pore pressure exhibits two peaks: 8.7 MPa at the tunnel wall after about 1 year and 10.3 MPa at the middle between two cells after about 200 years.

The distribution of pore pressure, as shown in Fig. 8, indicates that the gradient of pore pressure primarily emerges during the first year of heating (see Fig. 8(b)). In this relatively short duration, the rapid temperature increase, coupled with the low permeability of COx claystone, contributes to the appearance of this gradient and the first pore pressure peak.

Following this initial phase, as the temperature increase slows down, the overpressure zone has the opportunity to propagate into far field. This results in a decrease in pore pressure near the borehole wall and an increase in pore pressure farther from the borehole wall, as evident in Fig. 6-right and Fig. 8(c).

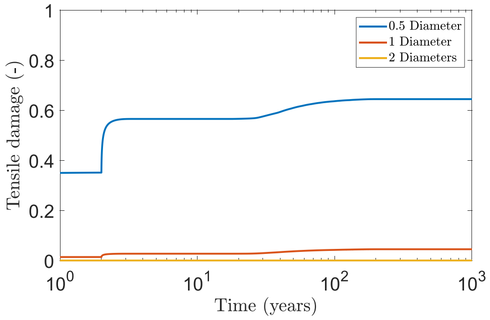

Fig. 10. Evolution of tensile damage at the different study points: 0.5 diameter, 1 diameter, 2 diameters (Case of 85-year cooling down).

The subsequent stage of pore pressure evolution begins around the 13th year. At this point, the pore pressure at the symmetric point reaches the same value as that at the 0.5 diameter point, indicating a nearly uniform pore pressure distribution across the horizontal extent of the study domain. And then, a second general increase in pore pressure occurs after this moment, initiated by temperature increases in the far-field, as shown in Fig. 8(d). As a result, the curves of pore pressure are almost coincided from this phase as shown in Fig. 6-right.

Finally, following the second pore pressure peak, the pore pressure gradually decreases from 200 to 1000 years. By the end of the simulation, the pore pressure value diminishes to 6.7 MPa, which remains higher than the initial pore pressure of 4.8 MPa.

The initiation of damage primarily arises from excavation and heating operations in this problem. In Fig. 9, the regions of shear damage and tensile damage resulting from excavation are displayed. This damage contributes to the formation of a borehole damaged zone (BDZ), a phenomenon commonly observed in in-situ experiments involving COx claystone [34,43].

The shear damage variable d^s reaches a maximum value of approximately 0.29 while the tensile damage variable d^t reaches 0.35, indicative of micro-cracking occurring exclusively around the boreholes, without significant macro-cracking. These micro-cracks result in heightened permeability.

Furthermore, experimental observations confirm that the onset of BDZ occurs horizontally around the borehole, situated within an almost isotropic initial stress field and the horizontal bedding plane of COx claystone. Remarkably, the simulation outcomes accurately replicate this phenomenon.

Throughout the heating phase, while the shear damage remains relatively constant, the evolution of tensile damage warrants further investigation. Fig. 10 illustrates the progression of tensile damage at

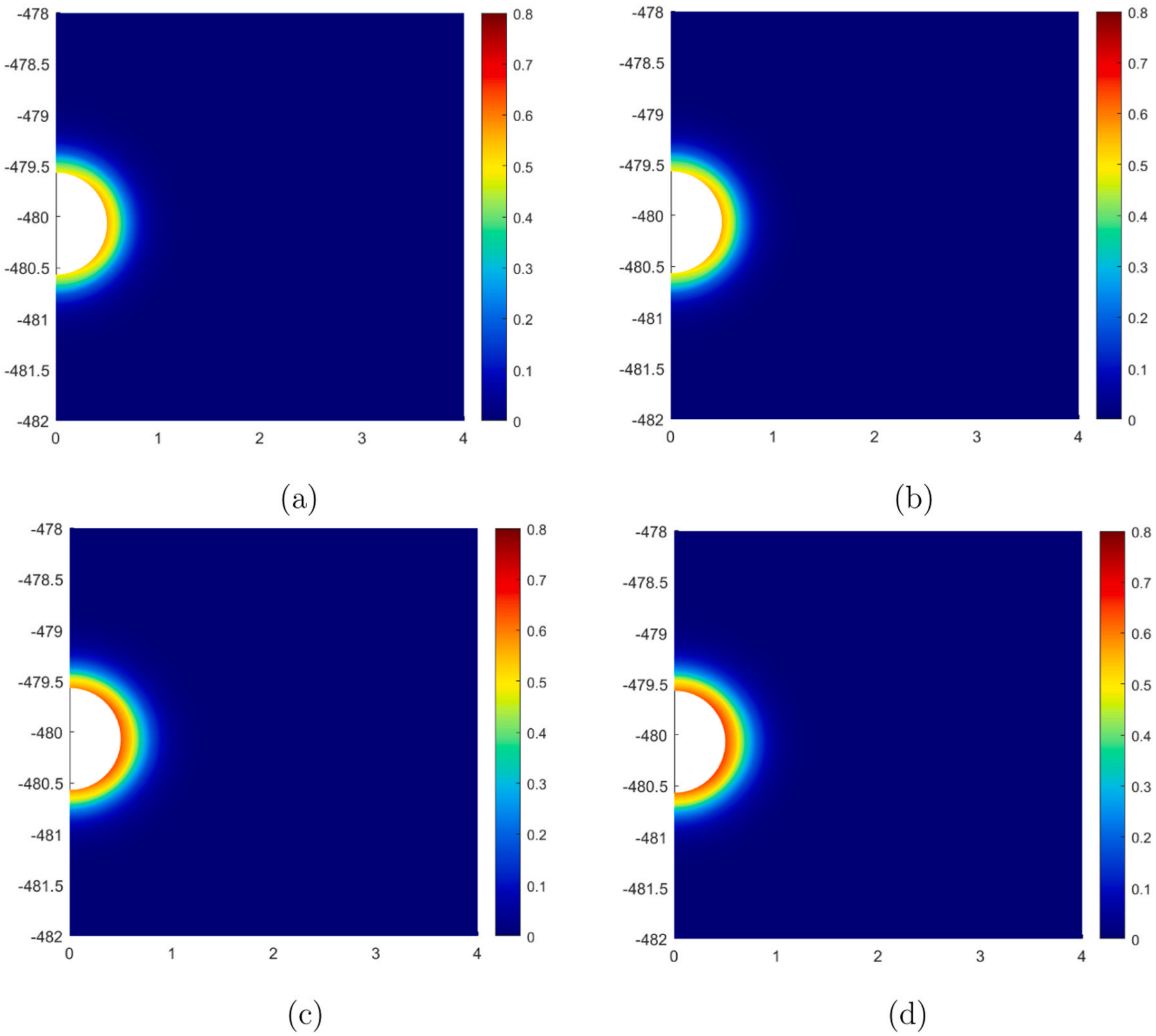

(a) (b) (c) (d)

Fig. 11. Distributions of tensile damage at different time of the heating phase: a) t = 1 year of heating; b) t = 13 years of heating; c) t = 48 years of heating; d) t = 1000 years of heating (Case of 85-year cooling down).

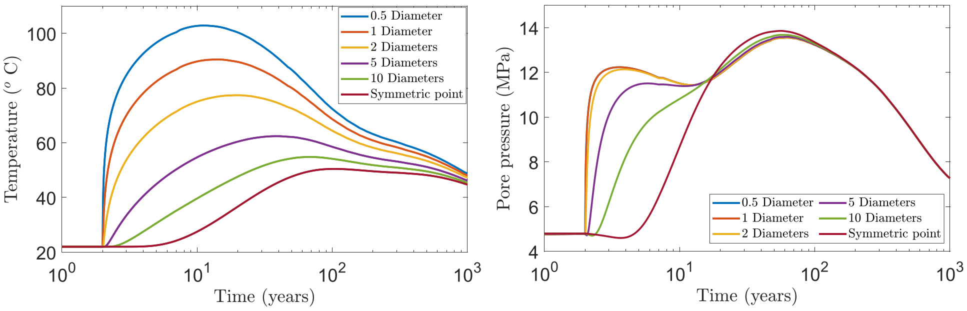

Fig. 12. Evolution of temperature (left) and pore pressure (right) at the different study points: 0.5 diameter, 1 diameter, 2 diameters, 5 diameters, 10 diameters and symmetric point (Case of 55-year cooling down).

three points in close proximity to the borehole. Comparing its behavior with temperature effects, the evolution of tensile damage appears more influenced by the increase in pore pressure.

At the moments of pore pressure elevation, the tensile damage at points located 0.5 and 1 diameter away experiences increments due to the rise in effective stress. Furthermore, Fig. 11 portrays the distribution of tensile damage at four distinct heating phases. Given the propagation of the tensile damage zone from the BDZ, which primarily extends horizontally, the heating-induced tensile damage is likewise concentrated in the horizontal direction after the first principal propagation, culminating at the 13th year.

Following the second principal propagation, which concludes around the 200-year, the tensile damage zone assumes an almost isotropic form. This transformation is attributed to the uniform distribution of pore pressure achieved over an extended period of heating.

Furthermore, to explore the impact of different HLW repository scenarios, we investigate the case where the HLW packages are installed in the study borehole after a wait of only 55 years. Employing the same

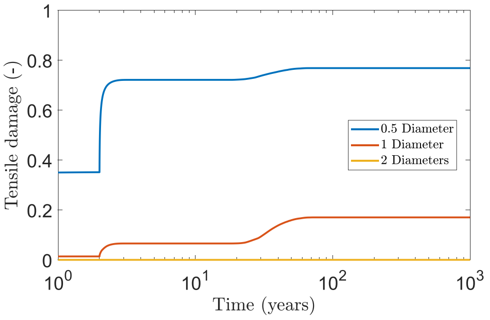

Fig. 13. Evolution of tensile damage at the different study points: 0.5 diameter, 1 diameter, 2 diameters (Case of 55-year cooling down).

visualization approach, Fig. 12 portrays the evolution of temperature and pore pressure over a 1000-year span at the same six study points.

Upon comparison with the 85-year case, the earlier onset of higher heating power leads to an increase in the temperature peak value, from 70˚C to 102˚C. Similarly, the two pore pressure peaks escalate, rising from 8.7 MPa to 12.5 MPa and from 10.3 MPa to 13.8 MPa. Nevertheless, the overall trends of the curves for both temperature and pore pressure exhibit minimal changes. The locations where the maxium pore pressure occurs do not change.

Figs. 13 and 14 depict the evolution and distribution of tensile damage throughout the heating phase in the 55-year scenario. Notably, the heating-induced tensile damage becomes more pronounced, with the maximum value of the tensile damage variable nearly reaching 0.8 by the end of the second increase.

Furthermore, in comparison with the 85-year case, the form of the tensile damage zone becomes isotropic at the end of the first increase. This shift is attributed to the more rapid increase in pore pressure in the 55-year scenario.

In summary, based on the simulation study of the long-term HLW repository problem, the occurrence of damage is primarily evident in three distinct stages. The damage induced by excavation aligns well with observations from in-situ tests. The damage resulting from heating manifests in both short-term and long-term coupling behaviors. The short-term coupling behavior arises due to the rapid escalation of temperature and pore pressure within the first year of heating. Conversely, the long-term coupling behavior emerges as a consequence of the gradual temperature increase in the far-field.

Upon comparing the simulation outcomes between the 85-year and 55-year scenarios, it becomes evident that if there is a desire to reduce the waiting time for HLW package installation, careful consideration must be given to managing the damage that intensifies during the initial year of heating. This aspect warrants dedicated investigation through pertinent in-situ tests.

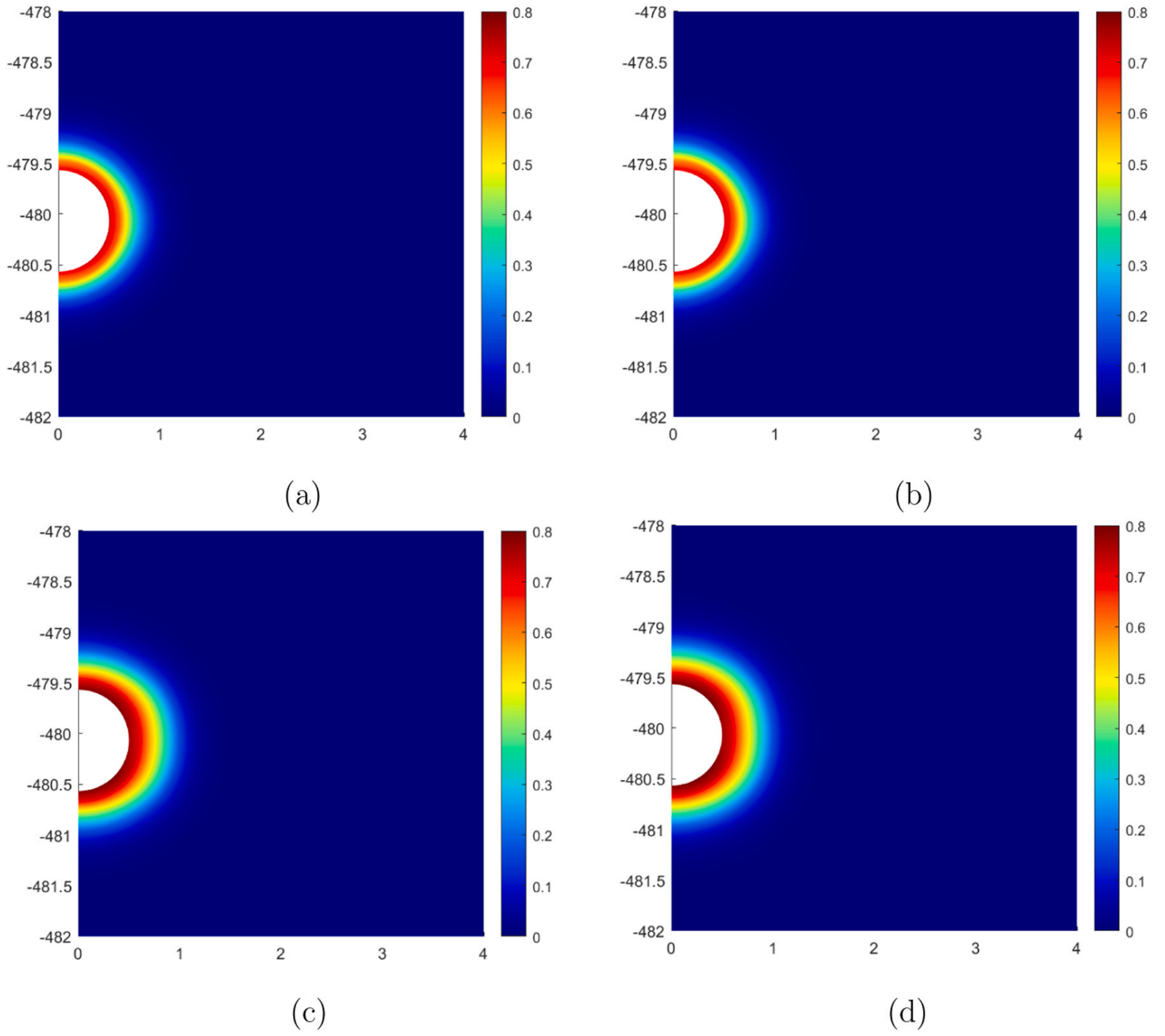

Fig. 14. Distributions of tensile damage at different time of the heating phase: a) t = 1 year of heating; b) t = 13 years of heating; c) t = 48 years of heating; d) t = 1000 years of heating (Case of 55-year cooling down).

6. Concluding remarks

Thermo-hydromechanical coupling is a crucial issue for short and long-term safety analysis of geological disposal of radioactive waste. The description of initiation and evolution of induced cracked zones is one of the most important aspects. Efficient and robust numerical methods should be developed for addressing such multi-physical problems. Among others, the phase-field method provides operational framework for modeling complex cracking processes by considering interactions between mechanical deformation, fluid flow and heat transfer.

The simulation provides a reasonable comparison between the two storage scenarios: 85-year and 55-year. In the case with the shorter waiting period for the package, a higher peak in temperature and pore pressure is observed during the heating process, leading to a more extensive hydro-thermal damage zone and consequently, an expanded BDZ. However, despite the gradual increase in temperature and pore pressure in the far field over 1000 years, the extension of damage remains limited to the near field in both storage scenarios. The presence of damage in the far field is likely more attributable to the boundary conditions on the far side, which are influenced by the distance between each two repositories.

In this paper, for the sake of page limitation, only saturated elastic porous rocks are considered. But the proposed framework has already been extended to partially saturated media with two-phase flow (water and gas), elastic-plastic materials.

In ongoing and future studies, self-sealing processes of induced cracks are investigated. Interactions between multiple components of disposal and their interfaces should also be considered.

Declaration of Competing Interests

The authors have no known competing financial interests or personal relationships that could have appeared to influence the work reported in this paper.

Acknowledgment

This work is jointly supported by the French National Agency for radioactive waste management (ANDRA) and the National Natural Science Foundation of China (No. 12202099).

Appendix A. Coefficient matrices for THM coupling problems

$$\begin{cases} \mathbf{R}_{uu} = \int_{\Omega} ({}^{t}\mathbf{B}_u)\mathbb{C}^b(d^t, d^s)\mathbf{B}_u dV \\ \mathbf{C}_{up} = \int_{\Omega} ({}^{t}\mathbf{B}_u)(-b(d^t))\mathbf{N}_p dV \\ \mathbf{C}_{uT} = \int_{\Omega}^{t} \mathbf{B}_u(-3\alpha_b K_b(d^t))\mathbf{N}_p dV \\ \Delta\mathbf{F}_e = \int_{S_t} ({}^{t}\mathbf{N}_u)\Delta\boldsymbol{t} dS + \int_{\Omega} ({}^{t}\mathbf{N}_u)\Delta\mathbf{f}_v dV \end{cases} \tag{42}$$

$$\begin{cases} \mathbf{R}_{pp} = \int_{\Omega} \left({}^{t}\mathbf{B}_p\right)\left(\boldsymbol{k}(d^t)/\mu\right)\mathbf{B}_p dV \\ \mathbf{M}_{pp} = \int_{\Omega} \left({}^{t}\mathbf{N}_p\right)\left(\frac{1}{M(d^t)}\right)\mathbf{N}_p dV \\ \mathbf{C}_{pu} = -{}^{t}\mathbf{C}_{up} \\ \mathbf{C}_{pT} = \int_{\Omega} \left({}^{t}\mathbf{N}_p\right)(-3\alpha_m(d^t))\mathbf{N}_p dV \\ \mathbf{F}_{\omega} = -\int_{S_{\omega}} \left({}^{t}\mathbf{N}_p\right)\mathbf{w}_{n+1}.\mathbf{n} dS \end{cases} \tag{43}$$

$$\begin{cases} \mathbf{R}_{TT} = \int_{\Omega} \left({}^{t}\mathbf{B}_p\right)\left(\frac{\lambda}{T_0}\right)\mathbf{B}_p dV \\ \mathbf{C}_{Tu} = -{}^{t}\mathbf{C}_{uT} \\ \mathbf{M}_{TT} = \int_{\Omega} \left({}^{t}\mathbf{N}_p\right)\left(\frac{C_{\sigma}^{b}}{T_0}\right)\mathbf{N}_p dV \\ \mathbf{C}_{Tp} = {}^{t}\mathbf{C}_{pT} \\ \mathbf{F}_q = -\int_{S_q} \left({}^{t}\mathbf{N}_p\right)\left(\mathbf{q}_{n+1}.\mathbf{n}/T_0\right) dS \end{cases} \tag{44}$$

$\mathbf{N}_u$ denotes the matrix of shape functions for approximation of displacement components, while $\mathbf{B}_u$ is the matrix of their derivatives to calculate the corresponding strain components. $\mathbf{N}_p$ is the matrix of shape function for approximation of fluid pressure or temperature, and $\mathbf{B}_p$ is the matrix of their derivatives to calculate the corresponding gradient components of fluid pressure or temperature.

B. Applied thermal loading history

Table 5
Applied heating power at different time steps.

Age (year)	Thermal load (kW)	Age (year)	Thermal load (kW)	Age (year)	Thermal load (kW)
0	106	55	24.2	200	4.49
1	97.4	60	21.9	210	4.28
2	91.1	65	19.9	220	4.14
3	86.1	70	18.1	230	4
4	82.3	75	16.5	240	3.89
5	79	80	15.1	250	3.78
6	76.4	85	13.9	260	3.69
7	73.9	90	12.8	270	3.6
8	71.4	95	11.8	280	3.52
9	69.3	100	11	290	3.45
10	67.6	110	9.53	300	3.39
15	59.2	120	8.4	400	2.86
20	52.1	130	7.48	500	2.45
25	46.6	140	6.72	600	2.1
30	41.4	150	6.13	700	1.81
35	37	160	5.67	800	1.56
40	33.1	170	5.29	900	1.35
45	29.8	180	4.96	1000	1.17
50	26.8	190	4.7	2000	0.33

References

[1] G. Armand, F. Bumbieler, N. Conil, R. dela Vaissiere, J.M. Bosgiraud, M.N. Vu, Main outcomes from in situ thermo-hydro-mechanical experiments programme to demonstrate feasibility of radioactive high-level waste disposal in the callovo-oxfordian claystone, J. Rock Mech. Geotech. Eng. 9 (2017) 415–427.

[2] Z.B. Liu, S.Y. Xie, J.F. Shao, N. Conil, Effects of deviatoric stress and structural anisotropy on compressive creep behavior of a clayey rock, Appl. Clay Sci. 114 (2015) 491–496.

[3] G. Armand, N. Conil, J. Talandier, D.M. Seyedi, Fundamental aspects of the hydromechanical behaviour of callovo-oxfordian claystone: from experimental studies to model calibration and validation, Comput. Geotech. 85 (2017) 277–286.

[4] G. Desbois, N. Hohne, J.L. Urai, P. Besuelle, G. Viggiani, Deformation in cemented mudrock (callovo-oxfordian clay) by microcracking, granular flow and phyllosilicate plasticity: insights from triaxial deformation, broad ion beam polishing and scanning electron microscopy, Solid Earth 8 (2) (2017) 291–305.

[5] M. Gasc-Barbier, S. Chanchole, P. Berest, Creep behavior of bure clayey rock, Appl. Clay Sci. 26 (2004) 449–458.

[6] M. Mohajerani, P. Delage, J. Sulem, M. Monfared, A.M. Tang, B. Gatmiri, A laboratory investigation of thermally induced pore pressure in the callovo-oxfordian claystone, Int. J. Rock Mech. Min. Sci. 52 (2012) 112–121.

[7] Z.B. Liu, S.Y. Xie, J.F. Shao, N. Conil, Multi-step triaxial compressive creep behaviour and induced gas permeability change of clay rich rock, Geotechnique 68 (2018) 281–289.

[8] Z.B. Liu, J.F. Shao, Moisture effects on damage and failure of claystone under compression, Geotech. Lett. 6 (2016) 1–5.

[9] H. Menaceur, P. Delage, A.M. Tang, N. Conil, The thermo-mechanical behaviour of the callovo-oxfordian claystone, Int. J. Rock Mech. Min. Sci. 78 (2015) 290–303.

[10] Z.B. Liu, J.F. Shao, S.Y. Xie, N. Conil, J. Talandier, Mechanical behavior of claystone in lateral decompression test and thermal effects, Rock Mech. Rock Eng. 52 (2019) 321–334.

[11] Z.B. Liu, J.F. Shao, S.Y. Xie, N. Conil, W. Zha, Effects of relative humidity and mineral compositions on creep deformation and failure of a claystone under compression, Int. J. Rock Mech. Min. Sci. 103 (2018) 68–76.

[12] P. Braun, S. Ghabezloo, P. Delage, J. Sulem, N. Conil, Theoretical analysis of pore pressure diffusion in some basic rock mechanics experiments, Rock Mech. Rock Eng. 51 (2018) 1361–1378.

[13] M.N. Vu, G. Armand, C. Plua, Thermal pressurization coefficient of anisotropic elastic porous media, Rock Mech. Rock Eng. (2019), https://doi.org/10.1007/s00603-019-02021-1.

[14] P. Braun, P. Delage, S. Ghabezloo, B. Chabot, N. Conil, M.N. Vu, Inducing tensile failure of claystone through thermal pressurization in a novel triaxial device, Rock Mech. Rock Eng. 55 (2022) 3881–3899.

[15] N. Conil, M. Vitel, C. Plua, M.N. Vu, D. Seyedi, G. Armand, In situ investigation of the thm behavior of the callovo-oxfordian claystone, Rock Mech. Rock Eng. 53 (2020) 2747–2769.

[16] F. Bumbieler, C. Plua, S. Tourchi, M.N. Vu, J. Vaunat, A. Gens, G. Armand, Feasibility of constructing a full scale radioactive high-level waste disposal cell and characterization of its thermo-hydro-mechanical behavior, Int. J. Rock Mech. Min. Sci. (2020) (submitted).

[17] C. Plua, M.N. Vu, R. de La Vaissiere, G. Armand, In situ thermal hydrofracturing behavior of the callovo-oxfordian claystone within the context of the deep geological disposal of radioactive waste in france, Rock Mech. Rock Eng. (2023).

[18] S. Tourchi, J. Vaunat, A. Gens, F. Bumbieler, M.-N. Vu, G. Armand, A full-scale in situ heating test in callovo-oxfordian claystone: observations, analysis and interpretation, Comput. Geotech. 133 (2021) 104045.

[19] D. Seyedi, G. Armand, N. Conil, M. Vitel, M.N. Vu, On the thermo-hydro-mechanical pressurization in callovo-oxfordian claystone under thermal loading, Poromechanics (2017) 754–761.

[20] M.N. Vu , D. Seyedi , G. Armand, 2015. Thermo-poro-mechanical coupled processes during thermal pressurization around nuclear waste repository. 6th Coupled Problems in Science and Engineering May 18–20, Venice, Italy.

[21] N. Moes, J. Dolbow, T. Belytschko, A finite element method for crack growth without remeshing, Int. J. Numer. Methods Eng. 46 (1999) 131–150.

[22] N. Moes, C. Stolz, N. Chevaugeon, P.E. Bernard, A level set based model for damage growth: the thick level set approach, Int. J. Numer. Methods. Eng. 86 (2010) 358–380.

[23] J. Oliver, Modelling strong discontinuities in solid mechanics via strain softening constitutive equations, part 1: fundamentales, Int. J. Numer. Methods Eng. 39 (1996) 3575–3600.

[24] Y. Sun, E. Roubin, J. Shao, J.-B. Colliat, Fe modeling of concrete with strong discontinuities for 3d shear fractures and comparison with experimental results, Eng. Fract. Mech. 251 (2021) 10775.

[25] Y. Sun, E. Roubin, J. Shao, J.-B. Colliat, Strong discontinuity fe analysis for heterogeneous materials: the role of crack closure mechanism, Comput. Struct. 251 (2021) 106556.

[26] Y. Sun, E. Roubin, J. Shao, J.-B. Colliat, Meso-scale finite element modeling of the fracture process zone evolution for concrete, Theor. Appl. Fract. Mech. 125 (2023) 103869.

[27] G.A. Francfort, J.-J. Marigo, Revisiting brittle fracture as an energy minimization problem, J. Mech. Phys. Solids 46 (8) (1998) 1319–1342.

[28] B. Bourdin, G.A. Francfort, J.-J. Marigo, Numerical experiments in revisited brittle fracture, J. Mech. Phy. Solids 48 (4) (2000) 797–826.

[29] C. Miehe, M. Hofacker, F. Welschinger, A phase field model for rate-independent crack propagation: robust algorithmic implementation based on operator splits, Comput. Methods Appl. Mech. Eng. 199 (45-48) (2010) 2765–2778.

[30] J. Fang, C. Wu, J. Li, Q. Liu, C. Wu, G. Sun, L. Qing, Phase field fracture in elasto-plastic solids: variational formulation for multi-surface plasticity and effects of plastic yield surfaces and hardening, Int. J. Mech. Sci. (2019).

[31] J. Choo, W. Sun, Coupled phase-field and plasticity modeling of geological materials: from brittle fracture to ductile flow, Comput. Methods Appl. Mech. Eng. 330 (2018) 1–32.

[32] M. Wang, F. Cormery, W. Shen, J. Shao, A novel phase-field model for mixed cracks in elastic-plastic materials incorporating unilateral effect and friction sliding, Comput. Methods Appl. Mech. Eng. 405 (2023) 115869.

[33] C. Miehe, M. Hofacker, L.-M. Schänzel, F. Aldakheel, Phase field modeling of fracture in multi-physics problems. part ii. coupled brittle-to-ductile failure criteria and crack propagation in thermo-elastic–plastic solids, Comput. Methods Appl. Mech. Eng. 294 (2015) 486–522.

[34] Z. Yu, J.F. Shao, M.N. Vu, G. Armand, Numerical study of thermo-hydro-mechanical responses of in situ heating test with phase-field model, Int. J. Rock Mech. Min. Sci. 138 (2021) 104542.

[35] M. Wang, W. Shen, J. Liu, J. Shao, Phase-field modeling of cracking process in partially saturated porous media and application to rainfall-induced landslides, Eng. Geol. 310 (2022) 106884.

[36] O. Coussy, Poromechanics, John Wiley & Sons, 2004.

[37] A.H.-D. Cheng, Poroelasticity, Vol. 27, Springe,, 2016.

[38] H. Amor, J.-J. Marigo, C. Maurini, Regularized formulation of the variational brittle fracture with unilateral contact: numerical experiments, J. Mech. Phys. Solids 57 (8) (2009) 1209–1229.

[39] R. Alessi, J.J. Marigo, S. Vidoli, Gradient damage models coupled with plasticity and nucleation of cohesive cracks, Arch. Ration. Mech. Anal. 242 (2014) 575–615.

[40] R. Alessi, J.J. Marigo, S. Vidoli, Gradient damage models coupled with plasticity: variational formulation and main properties, Mech. Mater. 80 (2015) 351–367.

[41] T.-F. Wong, Micromechanics of faulting in westerly granite, Int. J. Rock Mech. Min. Sci. Geomech. Abstr. 19 (2) (1982) 49–64.

[42] R. Wong, K. Chau, C. Tang, P. Lin, Analysis of crack coalescence in rock-like materials containing three flaws—part i: experimental approach, Int. J. Rock Mech. Min. Sc. 38 (7) (2001) 909–924.

[43] Z. Yu, J. Shao, G. Duveau, M.-N. Vu, G. Armand, Numerical modeling of deformation and damage around underground excavation by phase-field method with hydromechanical coupling, Comput. Geotech. 138 (2021) 104369.

[44] P. DeBuhan, L. Dormieux, On the validity of the effective stress concept for assessing the strength of saturated porous materials: a homogenization approach, J. Mech. Phys. Solids 44 (1996) 1649–1677.

[45] D. Lydzba, J.F. Shao, Stress equivalence principle for saturated porous media, Comptes Rendus Mecanique 330 (2002) 297–303.

[46] C. Miehe, F. Welschinger, M. Hofacker, Thermodynamically consistent phase-field models of fracture: variational principles and multi-field fe implementations, Int. J. Numer. Methods Eng. 83 (10) (2010) 1273–1311.

[47] B. Bourdin, G.A. Francfort, J.-J. Marigo, The variational approach to fracture, J. Elast. 91 (1-3) (2008) 5–148.

[48] Eurad wp7 hitec - milestone 49: Selection of benchmark exercises for task 2.3.2023.

[49] C. Plúa, M.-N. Vu, D.M. Seyedi, G. Armand, Effects of inherent spatial variability of rock properties on the thermo-hydro-mechanical responses of a high-level radioactive waste repository, Int. J. Rock Mech. Min. Sci. 145 (2021) 104682.

[50] C. Plúa, M. Vu, G. Armand, J. Rutqvist, J. Birkholzer, H. Xu, R. Guo, K. Thatcher, A. Bond, W. Wang, T. Nagel, H. Shao, O. Kolditz, A reliable numerical analysis for large-scale modelling of a high-level radioactive waste repository in the callovo-oxfordian claystone, Int. J. Rock Mech. Min. Sci. 140 (2021) 104574.

[51] M.J. Borden, C.V. Verhoosel, M.A. Scott, T.J. Hughes, C.M. Landis, A phase-field description of dynamic brittle fracture, Comput. Methods Appl. Mech. Eng. 217 (2012) 77–95.

[52] J.Y. Wu, V.P. Nguyen, C.T. Nguyen, D. Sutula, S. Bordas, S. Sinaie, S.P.A. Bordas, Chapiter one - phase field modeling of fracture, Adv. Appl. Mech. 53 (2020) 1–183.

[53] Z. Yu, J. Shao, Y. Sun, M. Wang, M. ngoc Vu, C. Plua, Numerical analysis of hydro-thermal fracturing in saturated rocks by considering material anisotropy and micro-structural heterogeneity, Int. J. Rock Mech. Min. Sci. 170 (2023) 105457.

Jianfu Shao is currently an exceptional-class professor at university of Lille. He has brought original contributions to theoretical development, experimental investigation and numerical modeling in the field of geomechanics, in particular on multi-scale approaches for thermo-hydromechanical problems. His research works are widely applied to various engineering problems such as geological disposal of radioactive waste, sequestration of CO2, storage of hydrogen, geothermal exploitation. He is an associated editor of two major international journals on rock mechanics and a member of editorial board for five other top international journals. He is the recipient of the Maurice A. Biot Medal (2022) for his seminal contributions to understanding the role of microstructure to macroscopic behaviour of porous materials. He is a member of the Academia Europaea.

Yu Zhan received his Bachelor's, Master's, and Ph.D. degrees from the University of Lille, France, in 2014, 2016, and 2019, respectively. He is currently a lecturer at the University of Lille. His primary research focuses are on the numerical modeling and simulation of fracture mechanics and the thermo-hydro-mechanical coupling effects in rock materials. His research is mainly applied in the field of nuclear waste disposal engineering. He has been involved in several international cooperation projects with the French National Agency for Radioactive Waste Management (ANDRA). Additionally, he has led one project funded by the National Natural Science Foundation of China and participated in two other projects funded by the same foundation.